Multi-frequency Jitter Detection and Modeling for Remote Sensing Satellite Platforms Using Non-collinear TDI CCD

ZHU Ying, *LI Xiaoqian**, *DONG Yanling*, *GUI Yuhao*, *LIAO Xiangjun*, *ZHANG Xin*

Hubei Key Laboratory of Optical Information and Pattern Recognition, School of Electrical and Information Engineering, Wuhan Institute of Technology, Wuhan 430205, P. R. China

(Received 3 June 2025; revised 17 September 2025; accepted 9 October 2025)

Abstract: The advancement of imaging resolution has made the impact of multi-frequency composite jitter in satellite platforms on non-collinear time delay and integration (TDI) charge-coupled device (CCD) imaging systems increasingly critical. Moreover, the accuracy of jitter detection is constrained by the limited inter-chip overlap region inherent to non-collinear TDI CCDs. To address these challenges, a multi-frequency jitter detection method is proposed, achieving sub-pixel level error extraction. Furthermore, a multi-frequency jitter fitting approach utilizing a scale-adjustable sliding window is introduced. For composite multi-frequency jitter, spectral analysis decomposes the relative jitter error curve, while the scale-adjustable sliding window enables frequency-division fitting and modeling. Validation experiments using Gaofen-8 (GF-8) remote sensing satellite imagery detected jitter at 0.65, 20, and 100 Hz in the cross-track direction and at 0.5, 100, and 120 Hz in the along-track direction, demonstrating the method's precision in detecting platform jitter at sub-pixel accuracy (<0.2 pixels) and its efficacy in fitting and modeling for non-collinear TDI CCD imaging systems subject to multi-frequency jitter.

Key words: remote sensing image matching; platform jitter; non-collinear TDI CCD; multi-frequency jitter fitting

CLC number: P237 **Document code:** A **Article ID:** 1005-1120(2025)05-0601-14

0 Introduction

Satellite platform jitter refers to the phenomenon of periodic micro-vibrations induced during on-orbit operations by disturbances, such as attitude adjustments, pointing control, solar panel deployments, and periodic movements of onboard moving components[1-2]. It is characterized by periodicity, micro-amplitude, difficulty in measurement, inherent nature, and challenging controllability[3]. With increasing imaging resolution, the impact of subtle platform jitter with minute amplitude on image quality has become increasingly significant. It has emerged as a core bottleneck restricting the geometric quality of imagery[4].

With the continuous advancement of high-resolution Earth observation technology, platform jitter has garnered growing attention globally. Numerous researchers domestically and internationally have conducted in-depth studies on the detection and modeling of satellite platform jitter-induced attitude errors, achieving notable results. Time-delayed integration imaging-based jitter detection methods represent a common approach for detecting satellite platform jitter. These methods exploit the parallax characteristics inherent in optical satellite time-delayed imaging or utilize reference data to capture the jitter pattern. Based on the detection results, a platform jitter model is constructed to convert the relative errors between images caused by jitter into absolute errors, thereby quantifying the specific impact of jitter on single-frame imaging accuracy[5-6]. The parallax between time-delayed integration images caused by platform jitter exhibits a distinct periodic varia-

*Corresponding author, E-mail address: xiaoqian_li@stu.wit.edu.cn.

How to cite this article: ZHU Ying, LI Xiaoqian, DONG Yanling, et al. Multi-frequency jitter detection and modeling for remote sensing satellite platforms using non-collinear TDI CCD[J]. Transactions of Nanjing University of Aeronautics and Astronautics, 2025,42(5):601-614.

http://dx.doi.org/10.16356/j.1005-1120.2025.05.004

tion pattern[7]. This enables the detection of jitter errors from time-delayed integration imagery, followed by fitting and modeling of the detected jitter errors[8]. Addressing jitter error detection for satellites with time-delayed imaging characteristics, Tong et al.[9] proposed a framework for jitter detection and compensation based on imagery, detecting jitter at approximately 0.67 Hz in the cross-track direction of Ziyuan-3 satellite images. While investigating jitter detection for Gaofen-1 02/03/04 satellites and considering the influence of internal sensor distortion on detection accuracy, Zhu et al.[10] were the first to discover jitter at frequencies of 1.1—1.2 Hz in the along-track direction. Liu et al.[11] proposed a method combining parallax observations with attitude data from attitude measurement sensors, experimentally detecting low-frequency jitter at 0.12 Hz in the along-track direction of China's Tiangong-1 satellite, with a jitter amplitude of about 6 pixels.

Prevalent multi-frequency jitter error modeling methods employ global fitting to handle low-frequency errors first, followed by secondary global fitting of the residuals[12]. While effective in characterizing low-frequency errors (typically large amplitude and slow variation), this approach suffers from the smoothing effect of global fitting when handling high-frequency jitter errors (typically small amplitude and rapid fluctuation), leading to the loss of high-frequency details and fitting distortion. It is hard to accurately fit the high-frequency components within multi-frequency jitter errors.

Typical time-delayed imaging types include multi-chip non-collinear time-delay and integration charge-coupled device (TDI CCD) cameras, multi-spectral band time-delayed imaging, and stereo imaging. For non-collinear TDI CCD imagery, the imaging angle difference between chips is smaller than that in stereo imaging[13]. For higher frequency jitter, the charge accumulation across multiple TDI CCD stages minimizes image motion caused by satellite platform jitter. This effect is more pronounced on higher-resolution panchromatic imagery, allowing direct detection on panchromatic images. Multi-spectral imagery exhibits lower spatial resolution compared to panchromatic imagery. Stereo imagery, due to large differences in imaging angles and significant influence from terrain undulation, presents large and complex parallax primarily caused by topography, making direct jitter detection difficult[14].

However, jitter detection and modeling for satellite platforms based on non-collinear TDI CCDs still face two core challenges. Firstly, the overlapping area (approximately 100 columns of pixels) between adjacent CCD chips is limited. Additionally, parallax fluctuations ranging from several to tens of pixels occur along the track direction due to terrain undulation. Consequently, platform jitter detection relies heavily on high-precision, highly reliable dense matching algorithms[15]. Secondly, sub-meter high-resolution satellites exhibit high sensitivity to platform jitter. Minute platform vibrations significantly impact imaging, often involving superimposed jitter across multiple frequency bands with a wide frequency span ranging from several hertz to hundreds of hertz, making high-precision modeling considerably difficult.

Existing methods addressing multi-frequency jitter error analysis and modeling for non-collinear TDI CCD imagery remains relatively scarce. Most studies fail to adequately consider the impact of multi-frequency jitter on detection and modeling precision and reliability. Generally, jitter that strongly impacts imaging quality is primarily concentrated below 100 Hz with larger amplitudes[16]. Consequently, detectable and fittable frequency components are predominantly low-frequency. However, with increasing satellite resolution, the impact of multi-frequency aliased jitter spanning a wide range on TDI CCD multi-stage integration imagery becomes increasingly significant. Che et al.[17] estimated Gaofen-8 satellite platform jitter using a high-precision dense matching error result and an established jitter-induced image shift estimation model based on error fitting analysis. They detected jitter at four frequencies (0.64, 19.74, 58.56 and 97.70 Hz) in the cross-track direction and three frequencies (0.17, 17.85 and 97.69 Hz) in the along-track direction. Hu et al.[18], focusing on the time-delayed imaging characteristics of China's Tiangong-1 satellite, proposed a high-frequency jitter detection method

based on dense matching and image registration error curves. They detected multiple jitter frequencies, finding concentrations at 0.689 5, 19.766 8, 58.611 0, and 97.685 0 Hz, and subsequently fitted and established a high-frequency jitter model.

Research on deep learning-based satellite platform jitter correction methods has also progressed in recent years. Wang et al.[19] proposed a progressive learning correction method for high-frequency jitter distortion in spaceborne TDI camera remote sensing images using generative adversarial networks, demonstrating superior performance over existing restoration methods on both simulated datasets and actual jitter-affected imagery. However, current deep learning research primarily addresses single-frequency satellite platform jitter and does not encompass the correction of multi-frequency jitter distortion.

This paper proposes a platform jitter detection and modeling method utilizing phase-based least squares combined matching and low-frequency global-high-frequency local modeling, based on the parallax imaging characteristics of non-collinear TDI CCDs. Firstly, for the jitter detection part, a high-precision dense matching method combining phase matching and least squares matching is proposed. This method effectively enhances matching accuracy through dynamic integer-pixel initial value propagation and sub-pixel optimization within small windows. Secondly, for the jitter modeling part, a frequency-decomposition fitting model is constructed to decompose aliased jitter frequencies into low-frequency global components and high-frequency residual components, enabling effective separation and modeling of multiple jitter frequencies.

1 Method

During satellite imaging, the motion of the platform prevents the imaging plane of each TDI CCD stage from maintaining geometric correspondence with the ground target. For non-collinear TDI CCD cameras, the CCDs are staggered on the focal plane. As shown in Fig.1, there is a distance of L rows (generally several thousand pixels) between two staggered CCDs along the track direction. The parallax between adjacent TDI CCD images in the along-track direction primarily originates from the physical distance between adjacent CCDs in that direction. An increase in this spacing leads to a longer imaging interval, consequently resulting in larger parallax. In the across-track direction, an overlapping region spanning C columns (typically around 100-pixel columns) creates a narrow overlapping area in the imaging region. The parallax in the cross-track direction is related to the overlap between adjacent images, and the smaller overlap leads to larger parallax[20].

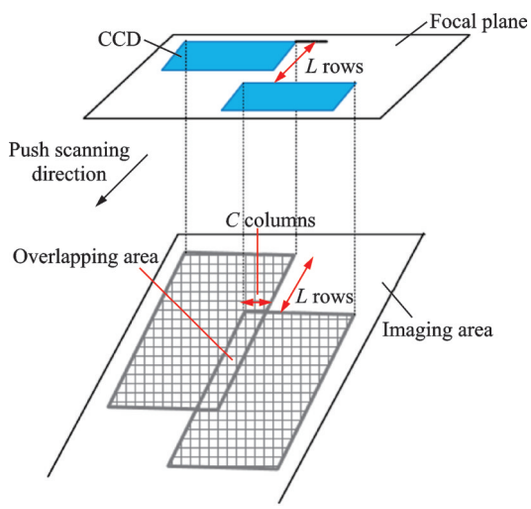

Fig.1 Schematic diagram of parallax imaging for the same ground object by adjacent non-collinear TDI CCDs under platform jitter conditions

Due to varying integration times, the degree of internal distortion caused by platform jitter also differs across spectral band images. Therefore, by analyzing the relative jitter errors between images within overlapping regions, the jitter behavior of the platform during imaging can be indirectly inferred, enabling the inversion of the platform's absolute jitter errors from the relative jitter errors[21]. The process begins with detecting the relative jitter errors between overlapping non-collinear TDI CCDs.

A dense matching process is performed on the images to obtain a parallax map between them. Analysis of this parallax map yields the relative jitter error curve. Subsequently, based on the relative jitter error detection results, spectral analysis is performed on the error curve, followed by fitting of the multi-frequency jitter errors. Finally, leveraging the

jitter attenuation characteristics of TDI CCD imagery, a rigorous parallax imaging model is constructed. Based on the relative jitter errors, multi-frequency absolute jitter errors are inverted, enabling precise absolute jitter error modeling for the imagery. The flowchart for the proposed multi-frequency jitter detection and modeling method based on non-collinear TDI CCDs is illustrated in Fig.2.

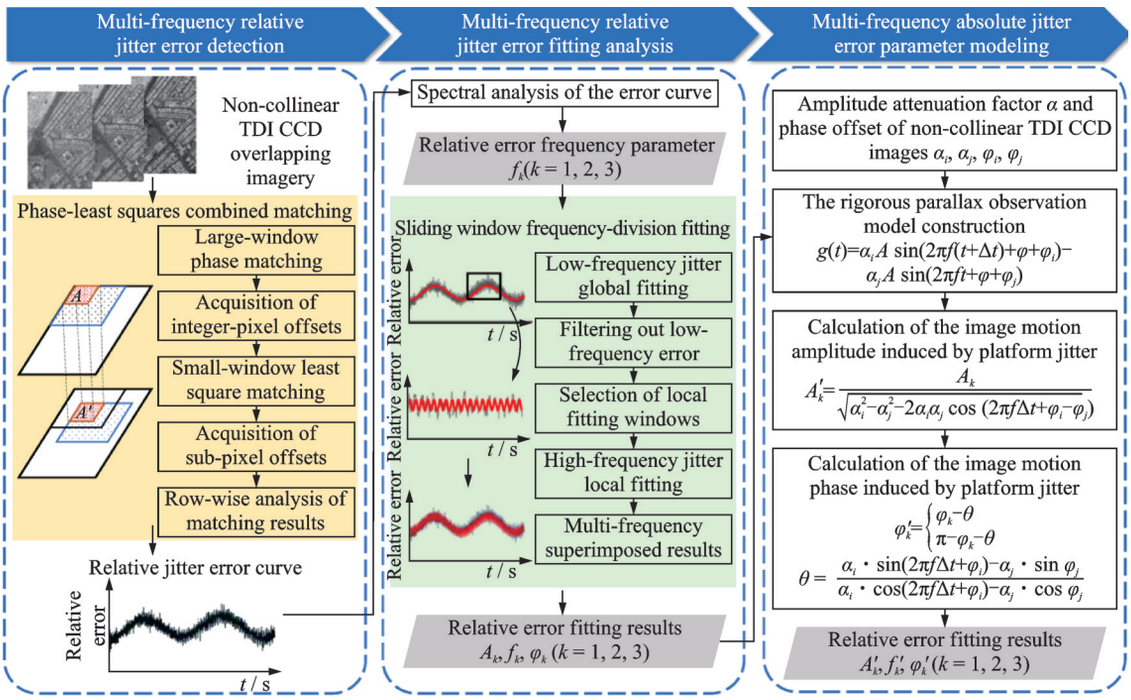

Fig.2 Flowchart of multi-frequency jitter detection and modeling based on non-collinear TDI CCDs

1.1 Jitter error detection based on imagery from limited overlap areas in non-collinear TDI CCDs

To acquire the registration errors induced by platform jitter with high precision, it is essential to rely on a high-accuracy, highly reliable dense matching algorithm to obtain dense homologous points for each scanning line in the time-delayed integration imagery. Utilizing a large number of observation points enhances the estimation accuracy of the registration errors. Commonly used high-precision dense matching methods include phase matching and least-squares matching. Phase matching can reflect the overall displacement of an image and typically requires a large window (e.g., 88 pixel × 88 pixel) to capture global information. However, under the limited overlap conditions of non-collinear TDI CCDs, a large window leads to an insufficient number of matching points, adversely affecting sub-pixel accuracy. Least-squares matching employs a small window, making it suitable for scenarios with limited overlap areas, offering numerous matching points and high precision. Nevertheless, under the imaging geometry of non-collinear TDI CCDs, the initial value between rows varies significantly, and a fixed initial value can easily lead to matching errors. Therefore, this paper proposes a jitter detection method based on imagery from the limited overlap areas of non-collinear TDI CCDs. By employing a phase-least squares combined matching algorithm, it integrates the advantages of both matching methods for image registration. On one hand, the improved phase matching provides accurate initial values and enables dynamic updating of these values, overcoming the issue of initial value variation. On the other hand, the least-squares matching leverages the advantage of small windows, ensuring a sufficient number of matching points even when the column-wise overlap is limited, thereby effectively improving registration accuracy.

Firstly, based on the TDI CCD design parameters, the initial row and column offsets for the left and right images are determined to locate the initial

position $(\Delta x, \Delta y)$ of the homologous points in the two image chips. Then, near this initial position, frequency-domain phase correlation matching is performed between a larger reference image window and the target image window to be matched. The position of the maximum correlation coefficient is calculated to obtain the integer-pixel displacement amounts, and the position of the homologous point is updated. This utilizes the global information in the frequency domain to effectively capture large-scale geometric offsets between the images, providing an accurate initial matching location $(\Delta x', \Delta y')$. Finally, at the position updated by the phase matching, a smaller fixed reference window is constructed in the reference image, while a corresponding target window is built in the image to be matched. Based on radiometric transformation and local affine geometric deformation, a grayscale error observation model between the two windows is established. An iterative optimization algorithm is employed to solve the model parameters, minimizing the sum of squared grayscale differences between the windows, thereby achieving sub-pixel matching results. The registration error of the kth homologous point in the nth scanning row is calculated as follows

$$\begin{cases} g_{x,k}^{n} = x_{i,k} - x_{j,k} - \Delta x' \\ g_{y,k}^{n} = y_{i,k} - y_{j,k} - \Delta y' \end{cases} \tag{1}$$

where $g_{x,k}^{n}$ and $g_{y,k}^{n}$ represent the registration errors in the cross-track and along-track directions, respectively; and $(x_{i,k}, y_{i,k})$ and $(x_{j,k}, y_{j,k})$ the coordinates of the kth homologous point in the nth row on the two CCD image chips i and j.

The registration error is calculated point-by-point for each matched homologous point, followed by a row-wise analysis. The average registration error for each row is statistically determined to derive the variation of registration error with respect to the imaging row (or imaging time), thereby obtaining the relative jitter error detection results, as expressed by the following equations

$$\begin{cases} g_x = [g_x^0, g_x^1, \cdots, g_x^{n-2}, g_x^{n-1}] \\ g_y = [g_y^0, g_y^1, \cdots, g_y^{n-2}, g_y^{n-1}] \end{cases} \tag{2}$$

where g_x^n represents the registration error in the cross-track direction within the overlapping area of the two adjacent CCD image chips at the nth row, and g_y^n the registration error in the along-track direction within the overlapping area of the two adjacent CCD image chips at the nth row.

1.2 Multi-frequency relative jitter error fitting based on scalable sliding window

To obtain initial estimates of the dominant frequencies and amplitudes of multi-frequency relative jitter errors in non-collinear TDI CCD systems, discrete Fourier analysis is employed to perform spectral analysis on the detected relative jitter error results. For multi-stage integration TDI CCD cameras, jitter can be classified into high-frequency jitter and low-frequency jitter based on the relationship between the total multi-stage integration imaging time $N\tau$ and the jitter period T. Jitter with a period shorter than the total integration time of the TDI CCD is referred to as high-frequency jitter, i.e., $N\tau f > 1$; jitter with a period longer than the total integration time is referred to as low-frequency jitter, i. e., $N\tau f < 1$. The jitter amplitude attenuation factor α follows the attenuation law of the absolute value of the sin$c$ function[5], expressed as

$$\alpha = |\sin c(N\tau f)| \tag{3}$$

Considering the characteristics of low-frequency jitter with larger amplitudes and high-frequency jitter with smaller amplitudes, low-frequency jitter can be directly fitted globally, while high-frequency jitter is not easily fitted directly. Therefore, to accurately obtain the parameters of different frequency components of the relative jitter error, this paper adopts a multi-frequency relative jitter error fitting method based on an adjustable-scale sliding window. The specific methodological workflow is as follows.

(1) Global low-frequency jitter fitting: Global fitting is performed for the low-frequency relative error components characterized by large amplitude and slow variation. Taking the cross-track direction as an example, a sinusoidal function is used as the fitting model. An observation equation is established for the average relative error of each scan line, and

the amplitude, frequency, and phase of the sinusoidal function are estimated using the least squares method. The objective of this stage is to capture the platform jitter error with larger amplitude, as represented as

$$v_1(t)=A_1\sin(2\pi f_1 t+\varphi_1)-g_x(t) \tag{4}$$

where t is the imaging time of the image, and $v_1(t)$ the fitting residual of the relative error in the across trajectory direction of the same point at time t; A_1, f_1, and φ_1 are the parameters to be solved for the fitting model of the relative error in the across-track direction are represented by amplitude, frequency, and phase, respectively; and $g_x(t)$ is the relative errors in the across-track direction at time t.

(2) Local high-frequency jitter fitting: After filtering out the modeled low-frequency component from the original relative error, local fitting is applied to the remaining high-frequency relative error components. Small-scale windows can accurately capture the minor variations of high-frequency jitter components. Similarly, a sinusoidal function model is applied within these small windows for precise fitting, enabling accurate characterization of local high-frequency details, as represented in

$$W(t_c,\Delta t)=\{t|t_c-\Delta t\leqslant t\leqslant t_c+\Delta t\} \tag{5}$$

where t_c is the center time of the window, determined by the maximum energy position of the residual at the initial estimated frequency; and Δt is the half width of the initial window and can be adaptively scaled according to the frequency.

(3) Multi-frequency error synthesis: Following the order of increasing frequency, the fitting for all frequency bands is sequentially completed. The low-frequency fitting results are then integrated with the high-frequency fitting outcomes derived from each small-scale window. This synthesis ultimately constructs a comprehensive multi-frequency relative error model capable of simultaneously characterizing both low-frequency and high-frequency error components.

1.3 Parameter modeling of multi-frequency absolute jitter errors based on relative jitter errors

For a non-collinear TDI CCD push-broom imaging camera, the satellite platform jitter is denoted as $d(t)=A\sin(2\pi ft+\varphi)$, where A, f, and φ represent the amplitude, frequency, and initial phase of the per-stage integration imaging jitter error, respectively. The rigorous parallax imaging model can be expressed as

$$g(t)=d(t+\Delta t)-d(t)=\alpha_i A\sin(2\pi f(t+\Delta t)+\varphi+\varphi_i)-\alpha_j A\sin(2\pi ft+\varphi+\varphi_j) \tag{6}$$

where $g(t)$ represents the relative jitter error between non-collinear TDI CCD images, and $d(t)$ the absolute jitter error between overlapping non-collinear TDI CCD images.

When the relative jitter error between overlapping non-collinear TDI CCD images is known, the amplitude, frequency, and initial phase of the absolute jitter error for per-stage integration imaging can be inverted through the rigorous parallax imaging model, as shown in Eq.(6). Therefore, we can model the amplitude and phase of absolute jitter error for TDI CCD image with multistage integration using the amplitude attenuation factor and phase offset through Eq.(6).

(1) Amplitude of per-stage integration imaging jitter error for TDI CCD imagery

Based on the periodicity and motion synthesis characteristics of platform movement, the frequency of the absolute jitter error in per-stage integration imaging should be consistent with the frequency of the relative jitter error. Combining this with the rigorous parallax imaging model yields the relationship between the relative jitter error of two multi-stage integration multispectral images and the amplitude of the absolute jitter error in per-stage integration imaging, expressed as

$$A'_k=\frac{A_k}{\sqrt{\alpha_i^2-\alpha_j^2-2\alpha_i\alpha_j\cos(2\pi f\Delta t+\varphi_i-\varphi_j)}} \tag{7}$$

When the integration level of two band images is the same ($\alpha_i=\alpha_j=\alpha$), there is

$$A'_k=\frac{A_k}{\alpha\sqrt{2-2\cos(2\pi f\Delta t)}}=\frac{A_k}{2\alpha|\sin(\pi f\Delta t)|} \tag{8}$$

(2) Single stage integrated imaging jitter error phase of TDI CCD image

Let $a=\cos(2\pi f\Delta t+\varphi_i)$, $b=\sin(2\pi f\Delta t+\varphi_i)$, $c=\cos\varphi_j$, $d=\sin\varphi_j$. According to the trigonometric

formula, we can obtain

$$g_{\mathrm{TDI}}(t)=A_k\sqrt{\alpha_i^2+\alpha_j^2-2\alpha_i\alpha_j\cos(2\pi f\Delta t+\varphi_i-\varphi_j)}\cdot \sin(2\pi ft+\varphi+\theta) \tag{9}$$

Therefore, the phase relationship between the relative jitter error and the absolute jitter error of per-stage integration imaging is given by

$$\theta=\arctan\left(\frac{\alpha_i\sin(2\pi f\Delta t+\varphi_i)-\alpha_j\cdot\sin\varphi_j}{\alpha_i\cos(2\pi f\Delta t+\varphi_i)-\alpha_j\cdot\sin\varphi_j}\right) \tag{10}$$

$$\varphi_k'=\begin{cases}\varphi_k-\theta\\ \pi-\varphi_k-\theta\end{cases} \tag{11}$$

When the number of TDI stages is identical for both band images, i.e., $\alpha_i=\alpha_j=\alpha$, $\varphi_i=\varphi_j=\Delta\varphi$, the following relationship holds

$$\varphi_k'=\begin{cases}\varphi_k-\Delta\varphi-\theta\\ \pi-\varphi_k-\Delta\varphi-\theta\end{cases}\quad \theta=\frac{\pi}{2}+\pi f\Delta t \tag{12}$$

Therefore, given the platform jitter frequency, the camera's line integration time, the number of TDI stages for the images, as well as the amplitude and phase of the relative jitter error between overlapping non-collinear TDI CCD images, the frequency, amplitude, and initial phase of the per-stage integration imaging jitter error can be inverted using Eqs.(7, 10). This enables the modeling of absolute jitter errors for TDI CCD overlapping images with different integration times and TDI stages.

2 Experiment and Analysis

2.1 Experimental data

The experiment presented in this paper utilized imagery data from the Gaofen-8 remote sensing satellite, with an image size of 6 144 pixel × 64 801 pixel. The Gaofen-8 satellite is a core optical remote sensing platform within China's high-resolution Earth observation system. Its onboard optical camera employs a non-collinear TDI CCD design. Adjacent TDI CCD images captured by the Gaofen-8 satellite exhibit a significant pixel displacement of 4 703 pixels. Concurrently, the overlap area between them is relatively narrow, comprising only 116 pixels. The line integration time was set to 0.066 238 ms. By analyzing these data, the specific impact of non-collinear TDI CCD design on image quality and registration accuracy can be further explored.

The experimental GF-8 imagery used in this study covers areas containing multiple typical land cover types, including urban building areas, farmland, and mixed woodland. Although the number of samples for each specific land cover type within the current dataset varies, our experimental results demonstrate that the proposed jitter detection method maintains stable performance across these different terrains. A systematic validation specifically targeting a wider range of land cover types will be a focus of our future work.

2.2 Analysis of platform jitter detection results

The data used for jitter detection consisted of four adjacent TDI CCD images, numbered 1, 2, 3, and 4, which were free from cloud interference. To detect the image errors induced by jitter, we leveraged the overlapping areas between these images to construct three pairs of time-delayed integration imagery. Especially, the overlapping area between these adjacent CCD chips is limited. Registration error analysis was performed on the overlapping areas of image pairs 1-2, 2-3, and 3-4, respectively. Subsequently, jitter detection was conducted on these three image pairs using the phase-least squares combined matching method.

By comparing the inter-piece registration errors, the image errors caused by platform jitter were obtained. The detection results are shown in Fig.3. It can be observed that the registration errors, both in the along-track and across-track directions, exhibit periodic variations. Furthermore, the three datasets show a highly consistent trend in their variation trends.

The Fourier analysis results indicate that both the across and along track directions contain three frequency components, but their specific compositions differ significantly. Among them, the across-track direction mainly includes three frequency components from low to high, namely 0.65, 20, and 100 Hz, while the main frequencies along the track direction are 0.5, 100, and 120 Hz, as shown in Fig.4.

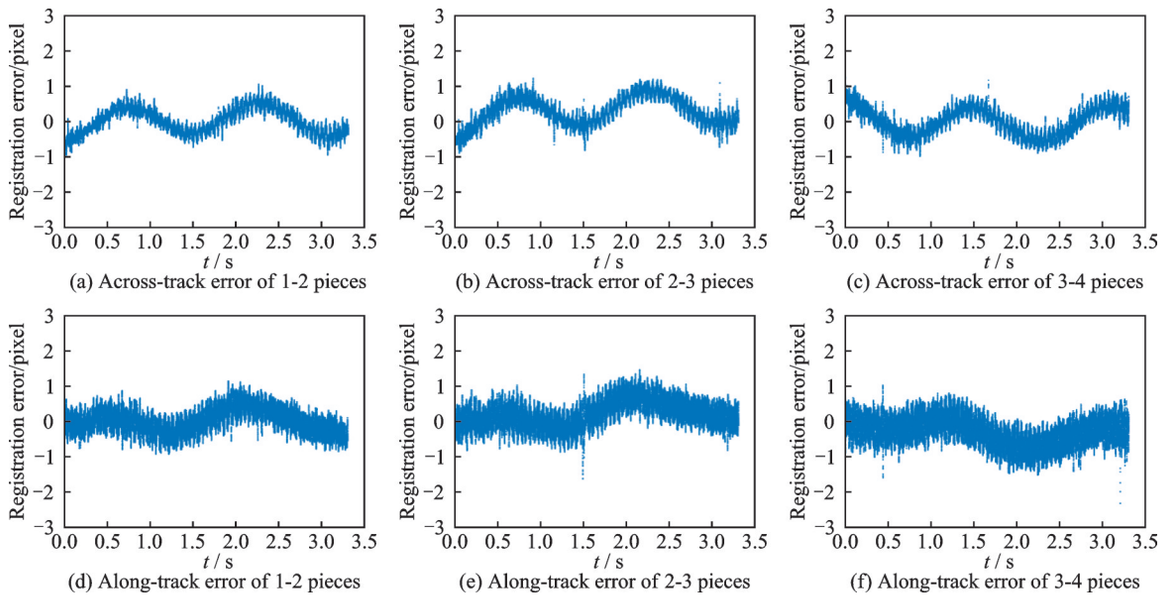

Fig.3 Registration error curves of 1-2, 2-3, 3-4 pieces in across-track direction and along-track direction

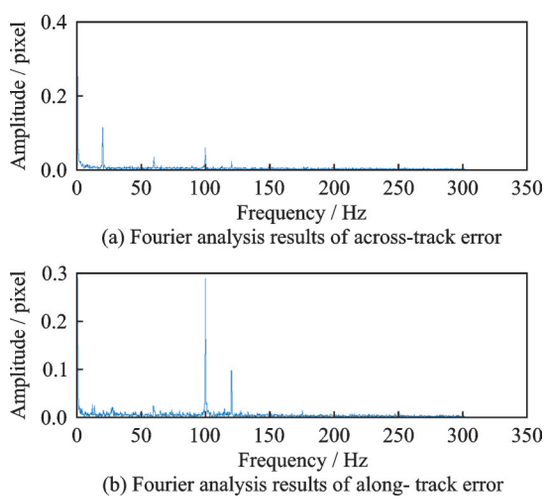

Fig.4 Fourier analysis results of across-track error and along-track error

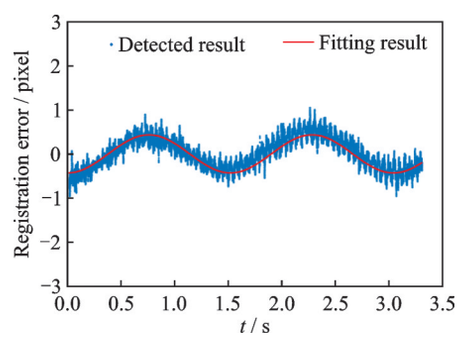

Fig.5 0.65 Hz error fitting curves of 1-2 pieces

2.3 Comparative analysis of platform jitter fitting

The multi frequency relative error curves detected between adjacent pieces (1-2 pieces) of Gaofen-8 satellite are fitted with jitter error using a scale adjustable sliding window. Firstly, overall fitting is adopted for the low-frequency jitter error of 0.65 Hz. When fitting the 0.65 Hz jitter, both the traditional method and the proposed method use the global fitting as shown in Fig.5.

When fitting to 20 Hz, adjust the fitting interval based on the scale adjustable sliding window model, select the relative error of 0.65 Hz from the imaging time (2—2.5 s) interval, remove the low-frequency error of 0.65 Hz, obtain the remaining error part, and perform error fitting. Finally, for the 100 Hz fitting, the fitting interval will be readjusted based on the scale adjustable sliding window model. Due to its higher frequency, a shorter interval (2—2.2 s) will be selected for fitting. After completing the frequency division fitting, in order to verify the accuracy of the fitting results, the fitting curves of different frequency components were superimposed and compared with the original relative error (blue curve). The frequency division fitting superposition result and the original error fitting result are shown in Fig.6.

In the fitting results for the 20 and 100 Hz errors, the traditional method exhibited lower accuracy in capturing the high-frequency components, with its fitted curve (red line) struggling to accurately represent the subtle variations of the high-frequen-

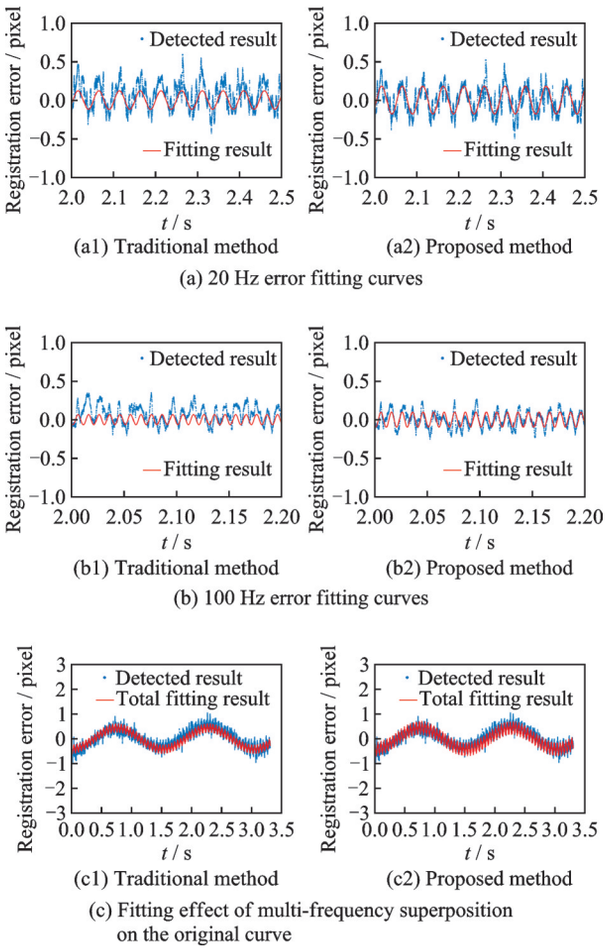

Fig.6 Comparison of the fitting effect of 1-2 relative errors between traditional and the proposed methods

cy errors. In contrast, the scalable sliding window method, employing a hierarchical fitting approach, closely aligns with the original error curve, effectively mitigating the smoothing distortions often associated with global fitting techniques.

2.4 Analysis of platform jitter modeling results

Adjust the high-frequency local fitting window and apply frequency division fitting method to accurately process the image combination of 2-3 pieces and 3-4 pieces, as shown in Figs.7, 8 and 9, respectively.

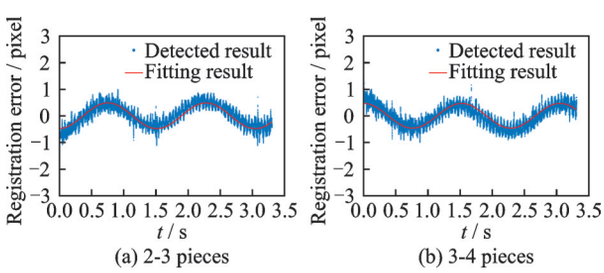

Fig.7 0.65 Hz error fitting of 2-3 and 3-4 pieces

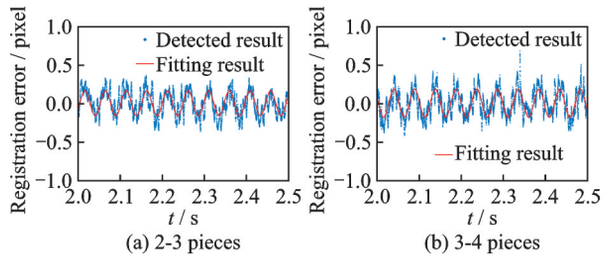

Fig.8 20 Hz error fitting of 2-3 and 3-4 pieces

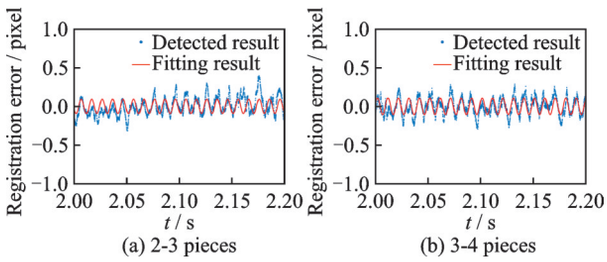

Fig.9 100 Hz error fitting of 2-3 and 3-4 pieces

The across-track registration errors were aggregated through superposition, and the resulting composite curve was compared with the original error curve, as shown in Fig.10. It can be observed that the superimposed fitted curve aligns almost perfectly with the original curve, demonstrating that the fitting process successfully captured the variation trends inherent in the raw data and achieved high precision in error fitting. After substituting the registration errors into the jitter model, the phase and amplitude information for the non-collinear TDI CCD panchromatic imagery was calculated, as summarized in Table 1.

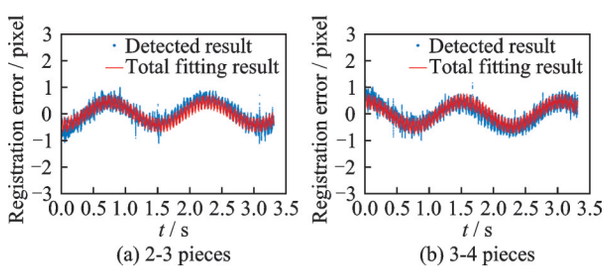

Fig.10 Fitting effect of multi-frequency superposition on the original curves of 2-3 and 3-4 pieces

Subsequently, the same methodology was applied to fit the along-track registration errors for the three combinations. Precise processing was performed on the image combinations of 1-2, 2-3, and 3-4 pieces, yielding the results shown in Figs.11—14, respectively.

Table 1 Fitting and absolute error estimation of multi-frequency registration error in across-track direction

Combination	Matching error			Absolute error		
	Frequency/Hz	Amplitude/pixel	Phase/rad	Frequency/Hz	Amplitude/pixel	Phase/rad
1-2	0.656 8	0.431 3	4.716 9	0.656 8	0.359 7	2.503 4
	20.447 8	0.181 7	0.117 1	20.447 8	0.099 0	2.615 6
	99.665 7	0.096 3	8.362 3	99.665 7	0.070 1	2.546 2
2-3	0.653 9	0.485 3	4.734 1	0.653 9	0.406 3	2.523 3
	20.390 5	0.162 7	0.904 1	20.390 5	0.091 0	1.772 5
	100.377 7	0.093 6	−1.088 9	100.377 3	0.062 5	2.777 4
3-4	0.654 5	0.466 1	1.577 6	0.654 5	0.390 0	0.647 3
	20.308 9	0.181 6	−1.123 3	20.308 9	0.106 2	2.563 1
	100.411 6	0.107 9	1.393 4	100.411 5	0.070 1	1.056 8

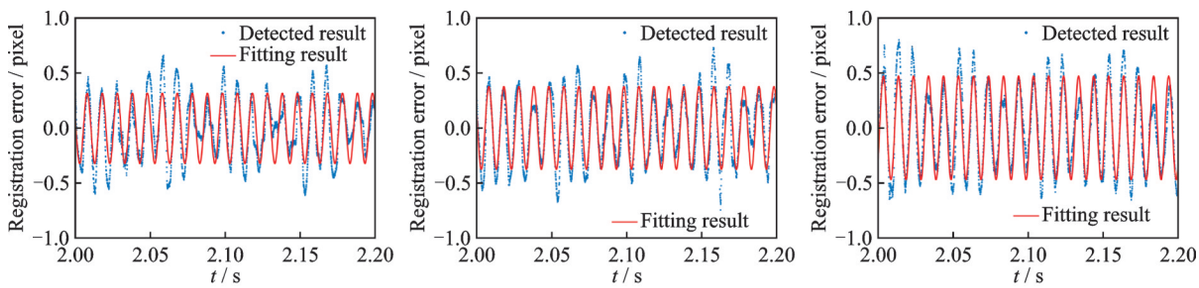

(a) 1-2 pieces (b) 2-3 pieces (c) 3-4 pieces

Fig.11 100 Hz error fitting of 1-2, 2-3, 3-4 pieces

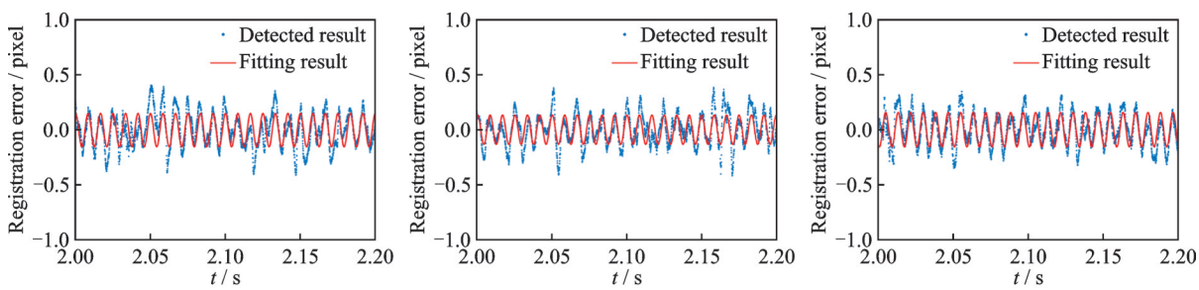

(a) 1-2 pieces (b) 2-3 pieces (c) 3-4 pieces

Fig.12 120 Hz error fitting of 1-2, 2-3, 3-4 pieces

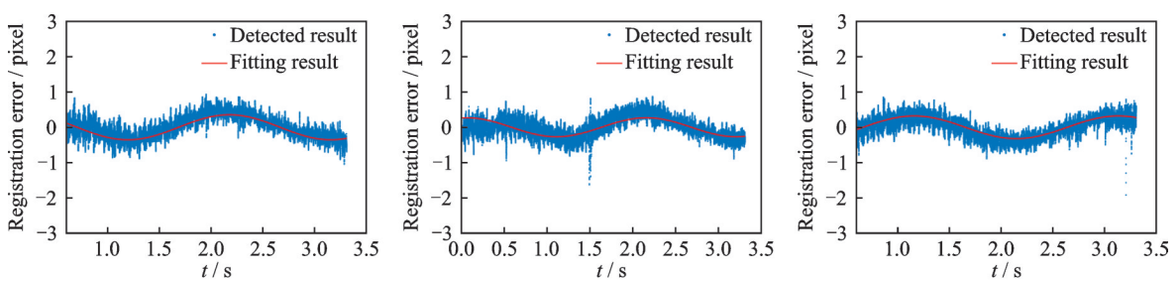

(a) 1-2 pieces (b) 2-3 pieces (c) 3-4 pieces

Fig.13 0.5 Hz error fitting of 1-2, 2-3, 3-4 pieces

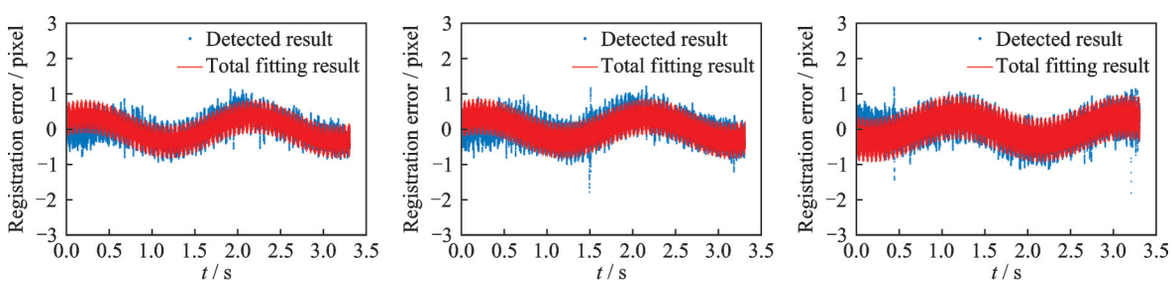

(a) 1-2 pieces (b) 2-3 pieces (c) 3-4 pieces

Fig.14 Overall fitting and comparison of registration errors in along-track direction

To accurately capture the error component at 100 Hz, we initially prioritized fitting the error at this specific frequency. Given its relatively large amplitude and rapid fluctuations, a local fitting strategy was employed to effectively capture the intricate details of this high-frequency error, presented in Fig.11. Subsequently, the 100 Hz error component was filtered out from the overall error signal. The residual data were then used to further fit the frequency error at 120 Hz and 0.6 Hz, with the fitted frequency information presented in Fig.12 and Fig.13. The along-track registration errors were aggregated through superposition and compared with the original error curve, as presented in Fig.14. It can be observed from Fig.14 that the superimposed fitted curve almost completely coincides with the original curve. This indicates that the fitting process successfully captured the variation trends of the raw data and achieved exceptionally high precision in error fitting, thereby validating the feasibility of the proposed method.

When validating the accuracy of the jitter modeling results, a comparative analysis of modeling outcomes from different chip combinations was conducted to ensure the reliability of the findings. Specifically, modeling results at identical frequencies were selected, and the differences between various chip combinations were calculated. Based on the registration errors and absolute errors provided in Tables 1 and 2 for the along-track and cross-track directions, combined with frequency and amplitude data, a further comparison of absolute jitter errors between different chip combinations was performed. The comparative results for the along-track and cross-track directions are presented in Tables 3 and 4, respectively.

Table 2 Multi-frequency registration error fitting and absolute error estimation along the track direction

Combination	Matching error			Absolute error		
	Frequency/Hz	Amplitude/pixel	Phase/rad	Frequency/Hz	Amplitude/pixel	Phase/rad
1-2	0.509 4	0.355 2	7.168 7	0.509 4	0.371 3	1.183 8
	99.918 3	0.319 7	3.800 2	99.918 3	0.413 6	2.626 2
	120.098 0	0.151 9	0.091 4	120.098 0	0.078 9	2.775 6
2-3	0.511 1	0.340 6	7.165 1	0.511 1	0.355 1	1.189 0
	99.976 8	0.375 9	3.120 2	99.976 8	0.428 6	2.003 4
	120.732 9	0.133 6	−8.092 1	120.732 9	0.071 0	1.462 0
3-4	0.506 8	0.322 5	4.145 2	0.506 8	0.338 8	3.070 4
	99.965 1	0.471 5	6.079 0	99.965 1	0.550 5	2.217 4
	120.176 0	0.157 4	1.830 8	120.176 0	0.080 2	1.632 6

Table 3 Differences in absolute error amplitude estimates of vibrations in across-track direction

pixel

Combination	Jitter in the cross-track direction		
	0.65 Hz	20 Hz	100 Hz
1-2 & 2-3	−0.046 6	0.008 0	0.007 6
1-2 & 3-4	−0.030 3	−0.007 2	0.000 4
2-3 & 3-4	0.016 3	−0.015 2	−0.007 6

Table 4 Differences in absolute error amplitude estimates of vibrations in along-track direction

pixel

Combination	Jitter in the along-track direction		
	0.5 Hz	100 Hz	120 Hz
1-2 & 2-3	0.016 2	−0.015 0	0.007 9
1-2 & 3-4	0.032 5	−0.136 9	−0.001 3
2-3 & 3-4	0.016 3	−0.121 9	−0.009 2

By calculating the error discrepancies between different chip combinations at identical frequencies, it can be observed that the differences in modeling results across-track direction are minimal. This outcome demonstrates that the jitter modeling method effectively detects jitter-induced effects in the imagery, and the modeling results exhibit a high degree of consistency across different chip combinations, thereby validating the methodological correctness and precision of the modeling approach. And it demonstrates the method's precision in detecting platform jitter at sub-pixel accuracy (<0.2 pixel) and its efficacy in fitting and modeling for non-collinear TDI CCD imaging systems subject to multi-frequency jitter.

The discrepancies in absolute error amplitude estimates across different chip combinations (Tables 3 and 4) primarily originate from: (1) The imaging time (TDI integration time) differs between different chips, and the platform jitter itself is not entirely stationary over time; and (2) the minor relative errors mainly originate from matching inaccuracies. Variations in the frequencies detected during matching lead to corresponding differences in the fitting and modeling outcomes. Despite these discrepancies, the differences for all frequency components are controlled within an acceptable range (all below 0.2 pixel). More importantly, the modeling results show consistent trends across different chip combinations, demonstrating the reliability of the proposed modeling approach.

To validate the superiority of the proposed method, a comparative analysis with three recent state-of-the-art platform jitter detection methods was conducted: (1) The jitter correction method based on a rigorous parallax observation model proposed by Zhu et al.[10], (2) the jitter distortion correction method using generative adversarial networks (GANs) proposed by Wang et al.[21], and (3) the traditional global fitting method mentioned previously for comparison. The comparison results are summarized in Tables 5 and 6. The comparative results indicate that the proposed scale-adjustable sliding window frequency-division fitting strategy significantly outperforms the existing methods in modeling accuracy for multi-frequency jitter, especially showing a distinct advantage in fitting high-frequency components.

Table 5 Performance comparison of fitting residuals in across-track direction pixel

Method	Jitter in the cross-track direction		
	0.65 Hz	20 Hz	100 Hz
Zhu et al.[10]	0.152 3	0.127 8	0.184 5
Wang et al.[21]	0.188 9	0.171 4	0.223 6
Traditional method	0.146 5	0.133 2	0.191 7
Proposed method	**0.082 1**	**0.071 5**	**0.089 3**

Table 6 Performance comparison of fitting residuals in along-track direction pixel

Method	Jitter in the along-track direction		
	0.5 Hz	100 Hz	120 Hz
Zhu et al.[10]	0.091 1	0.125 5	0.144 2
Wang et al.[21]	0.155 7	0.191 4	0.219 7
Traditional method	0.121 2	0.165 8	0.191 3
Proposed method	**0.078 4**	**0.092 7**	**0.095 8**

3 Conclusions

This study addresses the challenge of multi-frequency jitter detection and modeling, focusing on the insufficient robustness of traditional phase matching when applied to imagery with high-integration jumps or non-line-frequency normalization. An improved strategy featuring row-wise integer-pixel initial value propagation is proposed, effectively enhancing its stability and integer-pixel detection capability in L0-level imagery. Building upon this, the phase matching results are further utilized as initial values for refined matching. Combined with a gray-scale least squares observation model, a phase-least squares combined matching method is constructed, achieving sub-pixel error extraction that balances global robustness with local high precision. The accuracy and stability of the phase-least squares combined matching method were validated using real satellite data.

Concurrently, during the modeling phase, a frequency-decomposition fitting and modeling approach was adopted to achieve effective separation and modeling of multiple jitter frequencies. The superiority of the proposed method for multi-frequency jitter error detection was verified using non-collinear TDI CCD remote sensing imagery from the Gaofen-8 satellite. Through the fitting and analysis of errors at different frequencies, the proposed frequency-decomposition fitting strategy demonstrated significant advantages over traditional global fitting methods in precisely capturing high-frequency errors. This work provides theoretical support and experimental validation for the detection and precise modeling of platform jitter error in remote sensing imagery.

References

[1] ZHOU X Q, LIU H, LI Y, et al. Analysis of the influence of vibrations on the imaging quality of an integrated TDICCD aerial camera[J]. Optics Express, 2021, 29(12): 18108-18121.

[2] WAHBALLAH W A, ELTOHAMY F, BAZAN T

M. Influence of attitude parameters on image quality of very high-resolution satellite telescopes[J]. IEEE Transactions on Aerospace and Electronic Systems, 2021, 57(2): 1177-1183.

[3] WANG Mi, ZHU Ying, FAN Chengcheng. Development of platform jitter geometric analysis and processing for high-resolution optical satellite imagery[J]. Geomatics and Information Science of Wuhan University, 2018, 43(12): 1900-1904. (in Chinese)

[4] LI M H, ZHANG Z R, CHEN S Q, et al. Imaging simulation and learning-based image restoration for remote sensing time delay and integration cameras[J]. Transactions on Geoscience and Remote Sensing, 2023, 61: 1-17.

[5] ZHU Y, YANG T T, WANG M, et al. Rigorous parallax observation model-based remote sensing panchromatic and multispectral images jitter distortion correction for time delay integration cameras[J]. Transactions on Geoscience and Remote Sensing, 2024, 62: 6-18.

[6] ZHU Ying. Research on jitter processing methods for high resolution optical satellite imagery[D]. Wuhan: Wuhan University, 2016. (in Chinese)

[7] WANG Y L, ZHANG R H, XU Y Z, et al. Jitter error correction for the HaiYang-3A satellite based on multi-source attitude fusion[J]. Remote Sensing, 2025, 17: 2-15.

[8] ZHANG Z R, CHEN Z D, HU D, et al. Jitter-aware restoration with equivalent jitter model for remote sensing push-broom image[J]. Transactions on Geoscience and Remote Sensing, 2025, 63: 28-31.

[9] TONG X, YE Z, XU Y, et al. Framework of jitter detection and compensation for high resolution satellites[J]. Remote Sensing, 2014, 6(5): 3944-3964.

[10] ZHU Y, WANG M, CHEN Y, et al. An improved jitter detection method based on parallax observation of multispectral sensors for Gaofen-1 02/03/04 satellites[J]. Remote Sensing, 2018, 11: 16-23.

[11] LIU H, MA H, JJIANG Z, et al. Jitter detection based on parallax observations and attitude data for Chinese heavenly Palace-1 satellite[J]. Optics Express, 2019, 27: 1099-1103.

[12] PAN J, YE G, ZHU Y, et al. Jitter detection and image restoration based on continue dynamic shooting model for high-resolution TDI CCD satellite images[J]. Transactions on Geoscience and Remote Sensing, 2021, 59: 4915-4933.

[13] CAO Qipeng, DONG Xiaojing, HAN Xingzi, et al. Autonomous imaging parameters' adjustment for space TDI CCD camera[J]. Journal of Nanjing University of Aeronautics & Astronautics, 2019, 51(S): 73-77. (in Chinese)

[14] ZHANG H, LIU S, YE Z, et al. Effect of image window size on satellite jitter frequency detection[J]. ISPRS Congress, 2020, XLIII(B1): 149-153.

[15] TIAN Y Q, YU H J, ZHU Y. Jitter error detection and compensation method based on H-infinity filter fusion for remote sensing satellite image[C]//Proceedings of 2024 IEEE International Conference on Signal, Information and Data Processing (ICSIDP). Zhuhai, China: IEEE, 2024: 1-5.

[16] ZHOU X, LIU H, LI Y, et al. Analysis of the influence of vibrations on the imaging quality of an integrated TDI CCD aerial camera[J]. Optics Express, 2021, 29(12): 18108-18121.

[17] CHE Chengbang, FAND Zhonghao, PAN Jun, et al. Detection of GF-8 satellite platform jitter using multispectral imagery[C]//Proceedings of Academic Conference on High Resolution Earth Observation. [S.l.]: Wily, 2017: 846-859. (in Chinese)

[18] HU K, ZHANG Y, LIU W. High-frequency jitter detection by registration error curve of high-resolution multi-spectral satellite image[C]//Proceedings of International Conference on Geoinformatics. Kunming, China: IEEE, 2018: 1-6.

[19] ZHU Y, WANG H, WANG M, et al. Progressive learning-based jitter distortion correction for remote sensing images of time delay and integration camera [J]. Transactions on Geoscience and Remote Sensing, 2025, 63: 1-18.

[20] MO F, TANG X M, YANG Y B, et al. Preliminary Analysis of jitter detection and causes on the Ziyuan3 (ZY3) satellite series platforms[J]. Geoscience and Remote Sensing Letters, 2025, 22: 1-6.

[21] ZHENG L, JIN G, XU W, et al. Noise model of a multispectral TDI CCD imaging system and its parameter estimation of piecewise weighted least square fitting[J]. IEEE Sensors Journal, 2017, 17(12): 3657-3661.

Authors

The first author Dr. **ZHU Ying** received her B.S. degree in remote sensing science and technology in 2010 and her Ph.D. degree in photogrammetry and remote sensing in 2016, from Wuhan University, China. From 2017 to 2018, she was a postdoctoral researcher at School of Resource and Environmental Sciences, Wuhan University. From 2019 to 2020, she served as a specially appointed associate researcher at the State Key Laboratory of Information Engineering in Surveying, Mapping and Remote Sensing, Wuhan University. Since 2021, she has been with Hubei Key Laboratory of

Optical Information and Pattern Recognition, School of Electrical and Information Engineering, Wuhan Institute of Technology, where she is currently an associate professor. Her research interests include geometric processing of satellite remote sensing images, satellite jitter image analysis, image matching, and 3D modeling.

The corresponding author Ms. **LI Xiaoqian** received her B.Eng. degree in electronic information engineering from Wuhan Institute of Technology in 2024. In August 2024, she joined Hubei Key Laboratory of Optical Information and Pattern Recognition, School of Electrical and Information Engineering, Wuhan Institute of Technology as a postgraduate student. Her research primarily focuses on remote sensing image jitter detection and software design for remote sensing jitter analysis.

Author contributions Dr. **ZHU Ying** conceived and designed the study, developed the framework for detection and modeling, provided data for research analysis, and guided the improvement and revision of the research content. Ms. **LI Xiaoqian** conducted theoretical analysis, performed experimental validation based on the theoretical findings, and drafted the manuscript. Ms. **DONG Yanling** and Mr. **GUI Yuhao** participated in the experimental data analysis and content improvement of this study. Ms. **LIAO Xiangjun** and Mr. **ZHANG Xin** contributed to the discussion at stages of the research and provided background investigation. All authors commented on the manuscript draft and approved the submission.

Competing interests The authors declare no competing interests.

(Production Editor: ZHANG Huangqun)

基于非共线TDI CCD的摇感卫星平台多频震颤检测与建模

朱 映，李小倩，董彦玲，桂宇豪，廖祥君，章 鑫

(武汉工程大学电气信息学院光学信息与模式识别省重点实验室，武汉 430205，中国)

摘要：随着成像分辨率的提高，卫星平台多种频率叠加的震颤对非共线时间延时积分（Time delay and integration, TDI）电荷耦合元件（Charge-coupled device，CCD）成像系统的影响愈发显著，且非共线TDI CCD有限的片间重叠区域会限制震颤检测精度。因此，本文提出一种基于非共线TDI CCD有限重叠区域影像的多频震颤检测方法，并在此基础上提出了一种基于尺度可调滑动窗口的多频震颤拟合方法。首先，利用改进的相位-最小二乘联合匹配算法对震颤相对误差进行检测，实现亚像素级震颤误差提取；然后，针对多种频率叠加的震颤，通过频谱分析分解相对震颤误差曲线，并基于尺度可调滑动窗口对相对震颤误差曲线进行分频拟合和建模。采用高分八号（GF-8）遥感卫星影像开展的验证实验，在跨轨方向检测到0.65、20和100 Hz的震颤，在沿轨方向检测到0.5、100和120 Hz的震颤。实验结果表明，该方法对平台震颤的检测精度达到了亚像素级（<0.2像素），并能够有效完成在多频震颤影响下非共线TDI CCD成像系统的高精度拟合与建模。

关键词：遥感影像匹配；平台震颤；非共线TDI CCD；多频震颤拟合